Accepted Manuscript
Version of record at: https://doi.org/10.1149/1945-7111/ac76e1

Optimization of an Electrochemical Gas Separation and Inerting System

Utsav Raj Aryal[1] and Ajay K. Prasad[1†]

[1]Department of Mechanical Engineering, University of Delaware, Newark, DE 19716

Abstract

Aircraft fuel tank inerting is typically accomplished by supplying nitrogen enriched air (NEA) into the ullage (volume of air above the fuel level in the tank). We have developed a novel on-board electrochemical gas separation and inerting system (EGSIS) to generate NEA for fuel tank inerting. EGSIS is an electrically powered system that functionally combines a proton exchange membrane (PEM) fuel cell cathode with an electrolyzer anode. Water management is important in such a PEM-based system because proton transfer requires proper hydration of the membrane. Extremes of both dryout and flooding conditions should be avoided for optimal EGSIS performance. Previous single-cell EGSIS experiments revealed that supplying liquid water at the anode will maintain sufficient membrane hydration even when the system is operated under dry cathode conditions. However, it was difficult to avoid flooding at low cathode air stoichiometries when parallel flow field channels were employed. Here, we implement various strategies to optimize EGSIS performance such as using serpentine and interdigitated flow field channels, as well as a double-layer gas diffusion layer with graded hydrophobicity to mitigate flooding and improve water management. We also present a theoretical analysis of various stack configurations for a practical EGSIS module.

Keywords: Airplane fuel tank; Air separation; Inerting; Nitrogen-enriched air; Fuel cell; Electrolyzer; Optimization; Stack; Water management

† Corresponding author: email- prasad@udel.edu; Ph- 302 831 2960.

Accepted Manuscript
Version of record at: https://doi.org/10.1149/1945-7111/ac76e1

1. Introduction

Inerting is carried out in aircraft fuel tanks to prevent potentially catastrophic accidents such as the explosion of the air-fuel mixture in the ullage of TWA flight 800 in 1996[1]. An inert gas like nitrogen is typically supplied to the fuel tank to reduce its flammability by lowering the oxygen concentration in each ullage compartment to below 12 percent for commercial and 9 percent for military aircraft[2]. Current inerting techniques include on-board inert gas generation systems that produce nitrogen enriched air (NEA) through pressure swing adsorption or hollow fiber membrane modules. Such modules are costly, energy-intensive, undergo premature failure, and require pressurized air that increases the load on the engine compressor ultimately increasing fuel consumption and flight operating costs [3–9]. Another issue with such techniques is that the generation of NEA is more or less fixed. However, aircraft fuel tanks require inert gas supply at varying rates as determined by the aircraft's altitude, time of flight, and ullage volume. Compared to the ascent and cruise phases of the flight, a higher volume flowrate of NEA is required during the descent phase as the ullage volume increases with fuel consumption, and due to rising ambient pressure [9,10]. Hence, the design of the fuel tank inerting system is based on the inert gas flow required during the descent phase which makes conventional inerting systems heavy and expensive.

A novel on-board electrochemical gas separation and inerting system (EGSIS) has been demonstrated in our previous work [11–13] to address issues with incumbent technologies. EGSIS is an electrically powered device that functionally combines a proton exchange membrane (PEM) fuel cell cathode with an electrolyzer anode [14] to generate NEA and pure oxygen at the cathode and anode exit, respectively. The chemical reactions in an acidic electrolyte membrane EGSIS are:

$$H_2O \rightarrow \frac{1}{2}O_2 + 2H^+ + 2e^- \text{ (Anode)} \quad (1)$$

$$\frac{1}{2}O_2 + 2H^+ + 2e^- \rightarrow H_2O \text{ (Cathode)} \quad (2)$$

EGSIS is an electrochemical device such that each mole of water dissociated produces a half mole of oxygen at the anode. The anode reaction is exactly reversed at the cathode. The consumption of oxygen at the cathode reduces the oxygen concentration in the cathode air stream thereby generating NEA at its exit. Atmospheric oxygen is converted to water at the EGSIS cathode through the oxygen reduction reaction (ORR) as observed at the PEM fuel cell cathode. Similarly, the oxygen evolution reaction (OER) occurs at EGSIS anode as in the PEM electrolyzer. The protons (H^+) generated by the OER are transferred through the membrane from the anode to the cathode, whereas the electrons are transferred via the external circuit. The cathode outlet contains humidified NEA whose oxygen concentration lies within the safe limit, which can be passed through a water capture unit before entering the inerting space.

Accepted Manuscript
Version of record at: https://doi.org/10.1149/1945-7111/ac76e1

The Nernst potential for EGSIS would be zero if every reactant and product in both Equations 1 and 2 are kept under standard conditions as the anode reaction is the exact reverse of the cathode reaction. However, differences in the oxygen concentration at the anode and cathode imply that a non-zero Nernst potential is required for EGSIS operation. In practice, the applied voltage E_c must be large enough to overcome the activation, ohmic, and mass-transport overpotentials which exist in all electrochemical systems[15,16] including fuel cells and electrolyzers. A schematic of a single EGSIS cell is shown in Figure 1. A practical EGSIS would comprise a large number of cells assembled within a stack.

Efficient EGSIS operation requires careful system design, optimal operating conditions, and effective water management. Output indicators such as polarization curves and electrochemical impedance spectroscopy (EIS) measurements can be utilized to assess the influence of system design and operating parameters on overall performance and stability. Similar to other PEM-based systems, system design can include the use of various flow-field channels, gas diffusion layers (GDLs), catalyst layer compositions, and membranes, whereas operating conditions pertain to temperature, pressure, relative humidity, and reactant flowrates.

In particular, water management is important in any PEM-based system because proton transfer is facilitated by proper hydration of the membrane. Both drying and flooding conditions should be avoided for optimal EGSIS performance. In previous experiments, we showed that a single cell EGSIS employing parallel channels could produce NEA with as low as 5% oxygen concentration by reducing the air stoichiometry [11]. However, it was difficult to avoid flooding at low cathode air stoichiometries when parallel flow field channels were employed. Although better performance was observed at higher air flow rates, EGSIS needs to work effectively at fairly low stoichiometries in order to reduce the oxygen concentration in the NEA to the required inerting level. Hence, it is necessary to investigate other strategies to mitigate cathode flooding. Water can exist both in vapor and liquid states in an EGSIS cell. Water is a product of the electrochemical reaction at the cathode which can elevate the cathode relative humidity (RH) beyond the saturation limit causing flooding in the cathode catalyst layer and flow field channels. Moreover, liquid water is supplied to the anode inlet in our experiments. Since the water is in direct contact with the membrane on the anode side, it can diffuse easily to the cathode further elevating the cathode RH. Thus, suitable measures must be employed to optimize water management in EGSIS.

Water management has been studied extensively in fuel cells, for example by using different flow field channels such as serpentine and interdigitated instead of parallel channels [17–22], employing a double-layer gas diffusion media (GDM) with different hydrophobicities [23], and the use of water transport plates

Accepted Manuscript
Version of record at: https://doi.org/10.1149/1945-7111/ac76e1

(WTPs) to facilitate water removal and reduce water accumulation inside the cathode layer [24–26]. Such techniques can be employed in EGSIS as well to optimize water management and improve performance.

2. Experimental Procedure

Experiments were conducted using a single-cell EGSIS setup with an active area of 5 cm^2. Cathode flow field plates with three types of channels (parallel, serpentine, and interdigitated) were machined out of titanium. Only parallel titanium channels were used at the anode which was supplied with liquid water as the reactant. Silver-coated copper plates were used for current collection on both sides, and aluminum end plates were employed to compress the cell uniformly.

Nafion®-212 with 50 μm thickness was used for the experiments. The cathode electrode was a Vulcan carbon cloth loaded with 0.3 mg/cm^2 platinum catalyst whereas the anode catalyst (IrOx) was sprayed directly on the membrane for a uniform loading of 3 mg/cm^2. Details about the anode catalyst ink preparation and membrane electrode assembly (MEA) fabrication can be found in our earlier work [11]. The MEA was overlaid with Mylar gaskets on either side and then assembled between the flowfield plates and current collectors. The complete assembly was then compressed between the aluminum end plates using 8 bolts each torqued to 8.5 Nm. De-ionized (DI) liquid water was fed to the anode inlet using a syringe pump (New Era Pump Systems, model NE-1000HP) whereas dry air was supplied to the cathode from a compressed air tank as shown in Figure 2. The electrochemical tests were carried out with an Arbin Fuel Cell Test Station.

2.1 Reactant Flow

Assuming no side reactions occur, the reactant flowrates for water and air were calculated as follows. Faraday's law was used to determine the oxygen reduction rate at the cathode based on the current density drawn by EGSIS as:

$$\dot{n}_{O_2} = \frac{i}{4F} \tag{3}$$

where $\dot{n}_{O_2}$ (mol/cm^2s) in the molar flux of oxygen utilized, i (A/cm^2) is the current density, and F $(96485\ C/mol)$ is the Faraday constant. The air supply (mol/cm^2s) required for complete oxygen reduction when the oxygen mole fraction in air is χ_{O_2} can be calculated as [27]:

$$\dot{n}_{air} = \frac{i}{4\chi_{O_2}F} \tag{4}$$

If λ is the cathode air stoichiometry, Equation (4) can be written as:

Accepted Manuscript
Version of record at: https://doi.org/10.1149/1945-7111/ac76e1

$$\dot{n}_{air} = \frac{\lambda i}{4\chi_{O_2} F} \tag{5}$$

Similarly, the rate of consumption of water in $\mathrm{mol/cm^2 s}$ at the anode is:

$$\dot{n}_{H_2O} = \frac{i}{2F} \tag{6}$$

The water production rate at the cathode is identical to the water consumption rate at the anode. However, water transport also occurs from the anode to the cathode through the membrane by diffusion and electroosmotic flux. Hence, it is necessary to estimate the total flux of water through the membrane so that the water supply at the anode is adequate to maintain the OER after considering both diffusive flux and electroosmotic drag. The diffusion of water through the membrane can be determined in $\mathrm{mol/cm^2 s}$ using Fick's law[28]:

$$Flux_d = \frac{D_{w,F} C}{t}(a_a - a_c) \tag{7}$$

where $D_{w,F}$ $(\mathrm{cm^2/s})$ is the diffusion coefficient, C $(\mathrm{mol/cm^3})$ is the concentration of water in the membrane at standard state, a_a and a_c are the water activity values at the anode and cathode, respectively, and t (cm) is the membrane thickness. $D_{w,F}$ can be calculated as [29]:

$$D_{w,F} = (1.76 \times 10^{-5} + 1.94 \times 10^{-4}\lambda_w) e^{\left(\frac{-2436}{T}\right)} \tag{8}$$

where λ_w is the water content of the membrane and T (K) is the temperature. For our study, we have used $\lambda_w = 17$ as recommended by Springer et al.[30]. At this value of water content, we estimate $C = 7.8 \times 10^{-4}\ \mathrm{mol/cm^3}$ using the work of Majsztrik et al. [28,31]. Finally, a_a and a_c are taken as 1 and 0, respectively. Our assumption of a dry cathode, however, leads to a minor overestimation in $Flux_d$ which ensures that enough water is supplied to the anode at all times.

The water flux due to electroosmotic drag from anode to cathode in $\mathrm{mol/cm^2 s}$ is given by [30]:

$$Flux_{eo} = \frac{\eta_{drag} i}{F} \tag{9}$$

where $\eta_{drag} = \frac{2.5\lambda_w}{22}$ is the electroosmotic drag coefficient.

Equations (7-9) indicate that when $i = 1\ \mathrm{A/cm^2}$, $Flux_d < \dot{n}_{H_2O} < Flux_{eo}$. It should be noted that while $\dot{n}_{H_2O}$ and $Flux_{eo}$ are proportional to i, $Flux_d$ is independent of i. Thus, $Flux_d$ could exceed $\dot{n}_{H_2O}$ for very low current densities. However, $Flux_{eo}$ is always greater than $\dot{n}_{H_2O}$. Furthermore, the diffusive flux

Accepted Manuscript
Version of record at: https://doi.org/10.1149/1945-7111/ac76e1

is relatively small compared to the water consumption rate and electroosmotic flux. Hence, the over-estimation in $Flux_d$ due to the dry cathode assumption is not significant. The anode water supply needs to be greater than the sum of water consumed, and the diffusive and electroosmotic fluxes in order to reduce mass transport losses.

3. Results and Discussion

3.1 Effect of cathode gas diffusion medium and its hydrophobicity

Gas diffusion media (GDM) are the porous layers made from non-reactive material that facilitate uniform distribution of the reactants, electron transport, and water removal from the catalyst layers. The anode GDM material was platinized titanium to avoid corrosion whereas carbon cloth was used for the cathode. Here, we focus on the cathodic GDM to investigate cathode flooding and its mitigation. First, we present an experimental analysis to highlight the importance of an MEA with acceptable cell impedance. Both single-layer and double-layer cathode GDMs were tested. The single-layer GDM consisted of a 356 ± 15 μm thick gas diffusion electrode with 0.3 mg/cm^2 Pt catalyst containing around 30% polytetrafluoroethylene (PTFE) and a microporous layer (MPL), whereas the double-layer GDM consisted of an additional outer plain carbon cloth layer of 356 μm thickness. A comparison between the single- and double-layer GDMs is presented in terms of their polarization curves in Figure 3a. The cell temperature was maintained at 80℃, and the anode and cathode were supplied with 8 ml/hr of DI water and 400 sccm of dry air, respectively. The double-layer cathode GDM performed significantly better than the single-layer GDM as seen in Figure 3a. We conducted EIS measurements to understand this trend in performance. Figure 3b shows that the overall cell impedance decreased from 0.42 Ω for the single-layer GDM to 0.14 Ω for the double-layer GDM. The lower resistance for the double-layer GDL can only happen in the case of unoptimized torque leading to inadequate compression for the single-layer GDL case. The greater thickness of the double-layer GDM resulted in better compression which improved the electrical contact between the MEA and the flow field. Thus, the reduction in ohmic resistance is primarily responsible for the improved performance for the double-layer GDM seen in Figure 3a. Essentially, the double-layer GDL helps in minimizing contact resistance between the GDL/bipolar plate as well as GDL/catalyst layer interfaces.

Additionally, it has been reported that employing a GDM with graded hydrophobicity can mitigate cathode flooding and improve reactant transport [23]. In order to examine the effect of a graded hydrophobicity, experiments were conducted using carbon cloths with different PTFE content (0 to 30%) as the outer layer. The anode and cathode were supplied with 8 ml/hr of DI water and 150 sccm of dry air, respectively. The cell temperature was maintained at 60℃. 1.5 V was applied for a period of 5 hours during which the current density was recorded.

Accepted Manuscript
Version of record at: https://doi.org/10.1149/1945-7111/ac76e1

Figure 4(a) shows that EGSIS performance improves as the PTFE content of the outer GDM decreases, consistent with the finding of Wang et al.[23] who showed that the double-layer GDM with graded hydrophobicity reduces the overall saturation distribution by truncating the abruptly increasing saturation at the interface between the two layers. Consequently, the discontinuity in hydrophobicity achieved by decreasing the PTFE loading from the inner to outer GDM layer improves the transport of both water and oxygen because the more hydrophilic pores continue to extract water from the inner GDM while the more hydrophobic pores remain open for the reactant oxygen to pass through. The outer GDMs with 0 and 5% PTFE outperform those with 10, 20, and 30% PTFE. The outer GDM with 30% PTFE resulted in the lowest performance which was even lower than that obtained with no outer GDM. It has been reported that a higher PTFE loading within the GDM can reduce its electrical conductivity and lower performance [32]. Therefore, the cell impedance was measured for each case using EIS and the results are plotted in Figure 4(b). It can be seen that the cell impedance was similar for all double-layer GDMs (around 0.14 Ω) except for the 30% PTFE GDM which measured around 0.16 Ω. However, since the difference in these values is not significant, we attribute the difference in performance to the drop in hydrophobicity across the double-layer GDM.

PTFE content in the GDM needs to be optimized as well because a low PTFE content can result in poor water removal. Generally, the average PTFE content for optimal performance of electrochemical systems has been found to lie between 15 and 20% [33] which matches our results (the average PTFE loading for our case is 15% when the outer GDM has no PTFE). Thus, by creating a gradient in hydrophobicity from the inner to outer GDM by varying the PTFE loading, the double-layer interface results in better performance.

3.2 Effect of reactant flow rate and temperature

Water and air supply rates were varied in accordance with the calculations in Section 2.1 to examine their effect on current density and gain insight on water management in EGSIS. Parallel flow field channels were used on the anode and cathode for the results in Figures 5 and 6. A double-layer GDM was employed at the cathode where the outer GDL was a plain carbon cloth (1071 HCB) to reduce the contact resistance with the flow field as well as to improve water removal. We investigated the effect of varying the anode liquid water flowrate from 2-12 ml/hr while fixing the cathode dry air supply at 900 sccm in Figure 5(a). The cell temperature was maintained at 80℃. The cell was operated for 15 minutes at 0 V after which the voltage was raised to 1.5 V and the corresponding current density was measured for the next 30 minutes for each water flowrate.

Figure 5(a) shows that the current density is unstable and low at the low water flowrates of 2 and 4 ml/hr. At such flowrates, the water supplied is less than the sum of the water consumed, and diffusive

Accepted Manuscript
Version of record at: https://doi.org/10.1149/1945-7111/ac76e1

and electroosmotic fluxes. Hence, the cell suffers from mass transport losses. However, with increased water flowrates, the current density increases to a more or less constant value.

Next, we investigate the effect of varying the cathode air flowrate from 200-1200 sccm for a constant anode water flowrate of 8 ml/hr in Figure 5(b). The cell temperature was maintained at 80℃. The cell was initiated for 15 minutes at 0 V after which the voltage was raised to 1.5 V and the corresponding current density value was measured for the next 30 minutes. No air was supplied during the initialization phase, after which it was incremented as shown in Figure 5(b).

Figure 5(b) shows that the current density improves with the air supply rate. This improvement is partially because of higher stoichiometry. At higher stoichiometry, oxygen is more readily available at the catalyst sites and mass transport losses are minimized. Second, a higher air flowrate improves water removal. Water is not only produced at the cathode but is also transported from the anode through the membrane by diffusion and electroosmotic drag. If the water removal rate is insufficient, water will condense giving rise to liquid droplets that may cause flooding which will restrict the ORR by impeding oxygen access to the cathode catalyst sites leading to suboptimal performance, which is also observed in fuel cells [18,19]. Another conclusion from the above result is that membrane dryout is not a concern if liquid water is supplied to the anode, even when the cathode is operated at the highest airflow that severely reduces RH.

In order to further investigate the effect of flooding, current density values are compared for two flowrates and temperatures in Figure 6. The anode water flowrate was fixed at 8 ml/hr. Two cathode airflow rates of 120 and 600 sccm were employed for the 60℃ cell, whereas only 120 sccm was employed at 80℃. The voltage was incremented by 0.3 V from 0 to 0.6 V in 5-minutes steps followed by 0.1 V increments up to 1.6 V in 15-minute steps.

At the low air flowrate of 120 sccm for 60℃, the current density (black curve) increases with voltage until about 1.0 V. Thereafter, the current density declines and stagnates at around 0.2 A/cm^2 with increasing voltage. We attribute this fall in current density to cathode flooding. At the low flowrate and temperature of 120 sccm and 60℃, it is not possible to drive liquid water out of the cathode effectively. On the other hand, for the higher airflow rate of 600 sccm, the current density is seen to rise smoothly (blue curve). This again points to the detrimental effect of flooding at low airflow rates. However, at 80℃, such flooding behavior is not observed even at the low airflow rate of 120 sccm (green curve) because of the greater water carrying capacity of air at higher temperatures. Furthermore, at elevated temperatures, the temperature gradient from the catalyst layer to the flow channel increases the phase-change-induced flow

Accepted Manuscript
Version of record at: https://doi.org/10.1149/1945-7111/ac76e1

of water whereby liquid water vaporizes within the catalyst layer and condenses in the flow channels. The condensed water is then carried away from the flowfield by the airflow such that flooding is mitigated.

3.3 Effect of cathode flow field channels

Flow field design plays an important role in water management because the water transported across the GDM must be removed from the cell via the flow channels. Three canonical flow field channels are typically employed: parallel, serpentine, and interdigitated as shown in Figure 7(a). Diffusion is the only driving mechanism for the transport of both reactants and products in parallel channels, which can compromise mass transport. This can lead to the accumulation of liquid water in the channels and cause cathode flooding [19,20]. In contrast, adjacent channels in the serpentine design can experience a significant pressure drop which drives under-rib convection thereby enhancing oxygen supply to the catalyst sites and evacuating liquid water [21]. Similarly, interdigitated flow channels are dead-ended which also forces the gas through the porous GDM due to which the mass transport mechanism switches from diffusion to convection. Consequently, any liquid water surrounding the electrode is flushed out improving the performance [22].

Experiments were conducted to investigate the effect of the cathode flow field design. Parallel channels were used for the anode, whereas parallel, serpentine, and interdigitated channels were used for the cathode. The anode and cathode were supplied with 8 ml/hr of DI water and 150 sccm of dry air, respectively, while the cell temperature was maintained at 60℃. 1.5 V was applied to the EGSIS cell and the corresponding value of current density was recorded for 5 hours for each flow channel. As expected, Figure 7(b) shows that the parallel channel performs the worst of all three channels; the current density is the lowest and somewhat unstable over the 5 hr test. The interdigitated channel gave the best performance with the highest current density which was fairly stable. A stable current density was also observed for the serpentine channel whose performance was in between the parallel and interdigitated channels. Better performance for the interdigitated flow field channel can be attributed to effective liquid water evacuation from the cathode.

3.4 EGSIS stack configurations

A practical way to assemble any electrochemical device is to combine multiple cells in a stack to obtain modularity and scalability. Fuel cells are assembled in stacks to increase output voltage and power, whereas electrolyzers employ stacks for higher gas production rates. Wilkinson et al. [34] studied water management in solid polymer fuel cell stacks whereas Millet et al. [35] and Siracusano et al. [36,37] reported advances in electrolyzer stack design and optimization. Similarly, Selamet et al. [38] presentedthe development of a highly

Accepted Manuscript
Version of record at: https://doi.org/10.1149/1945-7111/ac76e1

efficient PEM electrolyzer stack, while Rashid et al. [39] and Riedel et al. [40] performed numerical and experimental analyses of solid oxide electrolysis stacks, respectively.

A practical EGSIS stack will include many cells to meet the actual NEA demand at the desired oxygen concentration. In our previous work with electrochemical compressor stack design [41], we coined two basic flow configurations as electrically in series/flow in parallel (ESFP), and electrically in series/flow in series (ESFS). These two configurations can be implemented for EGSIS as well as described next.

3.4.1 Electrically in series/flow in parallel (ESFP)

An EGSIS stack belongs to the ESFP configuration when all its cells are connected electrically in series whereas the gas flows through each cell in a parallel manner. Here, all anode inlets are plumbed together, as also all anode outlets, as shown in Figure 8(a). The cathode inlets and outlets are plumbed similarly. The inlet streams are divided equally and fed to each cell and are then collected and recombined at the outlet. The blue path represents water flow and the black path represents the air/NEA flow. The MEAs (blue) are sandwiched between the anode (orange) and cathode (green). Although the schematic depicts a stack of four cells, a practical stack may include many more cells. The voltage applied across the stack is equal to NE, where N is the number of cells in the stack, and E is the voltage across each cell.

In fact, an ESFP configuration with N cells, is equivalent to a large single cell with N times the MEA area as established for an electrochemical compressor stack [41] as well. However, a cell with large area is mechanically difficult to design and manufacture. Electrochemical gas separation and inerting occurs in a single pass through the cell in ESFP where atmospheric air is reduced to NEA. Due to its single-pass nature, the inlet air stoichiometry would need to be curtailed in order to achieve adequate inerting.

3.4.2 Electrically in series/flow in series (ESFS)

An EGSIS stack belongs to the ESFS configuration when all its cells are connected in series both electrically and flow-wise. Similar to the ESFP case, the external voltage applied at the stack terminals is divided equally across each cell in the ESFS case as well. However, as shown in Figure 8(b), the anode outlet from the first cell is fed to the anode inlet of the adjoining cell and this is continued throughout. The cathode outlets and inlets are plumbed similarly. Thus, the output air stream from the first cell's cathode becomes the input to the next cell's cathode and so on. Figure 8(b) also shows a stack of just four cells; however, a practical stack would include many more cells. The color scheme used in Figure 8(b) to depict the various components and flows is the same as in Figure 8(a).

An ESFS stack is in fact a multi-stage system where electrochemical gas separation and inerting occurs over repeated passes through the N cells such that the oxygen concentration is successively reduced

Accepted Manuscript
Version of record at: https://doi.org/10.1149/1945-7111/ac76e1

during each pass. Due to its multi-stage nature, the ESFS inlet air stoichiometry could be significantly larger than the ESFP case.

3.4.3 Stack Performance Comparison

EGSIS stacks belonging to the ESFP and ESFS configurations are compared in terms of their efficiency to convert a given flowrate of input air to NEA with a specified outlet oxygen concentration. An analytical expression for efficiency is derived based on the theoretical minimum power required to produce the required NEA and the actual electrical power utilized during the process. The theoretical minimum power required for a single EGSIS cell can be written as [11]:

$$P_{min} = \frac{RTI\left(1-\chi_{O_{2(out)}}\right)}{4F\left(\chi_{O_{2(in)}}-\chi_{O_{2(out)}}\right)}\left[\left\{\chi_{O_{2(in)}}\, ln\left(\frac{1-\chi_{O_{2(in)}}}{\chi_{O_{2(in)}}}\right) - ln\left(1-\chi_{O_{2(in)}}\right)\right\} - \left\{\chi_{O_{2(out)}}\, ln\left(\frac{1-\chi_{O_{2(out)}}}{\chi_{O_{2(out)}}}\right) - ln\left(1-\chi_{O_{2(out)}}\right)\right\}\right] \quad (10)$$

where R is the universal gas constant, T is the temperature, I is the current produced in the system, F is Faraday's constant, and $\chi_{O_{2(in)}}$ and $\chi_{O_{2(out)}}$ are the oxygen concentrations in the inlet air and outlet NEA, respectively.

The electrical energy applied to the EGSIS cell during this process is:

$$P_{electrical} = E \times I \quad (11)$$

where E is the voltage applied to the cell. Then, the efficiency can be calculated as:

$$\eta_{cell} = \frac{RT\left(1-\chi_{O_{2(out)}}\right)}{4FE\left(\chi_{O_{2(in)}}-\chi_{O_{2(out)}}\right)}\left[\left\{\chi_{O_{2(in)}}\, ln\left(\frac{1-\chi_{O_{2(in)}}}{\chi_{O_{2(in)}}}\right) - ln\left(1-\chi_{O_{2(in)}}\right)\right\} - \left\{\chi_{O_{2(out)}}\, ln\left(\frac{1-\chi_{O_{2(out)}}}{\chi_{O_{2(out)}}}\right) - ln\left(1-\chi_{O_{2(out)}}\right)\right\}\right] \quad (12)$$

The required theoretical minimum power and the electrical power applied for N cells in the ESFP configuration will be N times that of a single cell because each cell is operating under identical conditions. Therefore, the ESFP stack efficiency is also identical to the efficiency of a single cell. For the ESFS stack, the theoretical minimum power across each cell can be calculated using Equation (10) and summed to obtain the total minimum stack power, whereas the applied electrical power would be the same as that for the ESFP stack. The underlying assumption for this analytical comparison is that the current density remains the same for a given voltage irrespective of the configuration. In addition, we assume that the inlet of each

Accepted Manuscript
Version of record at: https://doi.org/10.1149/1945-7111/ac76e1

cell in the ESFS stack is dry in order to enable a proper comparison with the ESFP stack. This assumption is justified for two practical reasons. First, water needs to be recycled within EGSIS since the water produced at the cathode must be supplied back to the anode. Therefore, it is reasonable to consider the incorporation of a water capture module between each cell or between some subset of cells within the ESFS stack which will limit the moisture content in the ESFS cathode stream. Second, the NEA ultimately supplied to the fuel tank must be dry. Equation (12) was numerically investigated to obtain the efficiencies of the ESFP and ESFS stacks as a function of cell number. Figure 9(a) shows the results for calculated efficiency of ESFP and ESFS stacks containing 10 cells where the voltage applied to each cell is 1 V, and the oxygen concentrations at the air inlet and in the outlet NEA are 0.2 and 0.01, respectively. Figure 9(a) confirms that the efficiency does not vary across the ESFP stack and is equal to that of a single cell, whereas the efficiency of the ESFS stack increases monotonically from the first cell to the last. Similarly, each cell in the ESFP stack produces NEA with the specified outlet oxygen concentration which can then be combined to produce the total exit NEA flow. On the other hand, the oxygen concentration drops steadily from cell to cell across the ESFS stack producing the required NEA flow with the specified oxygen concentration at the outlet of the last cell.

Figure 9(a) indicates that the overall efficiency of the ESFS stack (1.478%) is lower than that of the ESFP stack (1.661%) for the stated conditions. In fact, it can be shown that the ESFP stack is more efficient than the ESFS stack for every condition. Although this analysis suggests that it is more efficient to run a stack in the ESFP configuration, there could be some practical considerations which favor the ESFS configuration. For instance, we have shown experimentally that the current density increases with the reactant flowrate, and since the ESFS stack runs with large initial flow rates, this could lead to improved efficiencies. Similarly, higher flow rates could mitigate cathode flooding and thereby improve stack performance. On the other hand, pumping losses would be much greater for the ESFS stack. Such practical considerations are beyond the scope of this analysis.

The steadily increasing slope of the efficiency curve across the ESFS stack in Figure 9(a) poses the interesting question as to what would happen for a stack with a much larger number of cells. To answer this question, we plot the efficiency of the first and last cell in the ESFS stack while varying the total number of cells from 1 to 1000 in Figure 9(b). For $N = 1$, $\eta = 1.661$ as expected for a single cell. For $N > 1$, the efficiency of the first cell begins to drop and plateaus to 0.796%. However, the efficiency of the last cell increases with N before plateauing to 3.255%. The efficiency rise of the last cell is steeper than the efficiency decline of the first cell. Interestingly, the overall ESFS stack efficiency decreases with N before plateauing to 1.462% for the given conditions.

ESFP and ESFS stacks could combined in different ways to obtain a hybrid configuration which combines the advantages of both systems either in terms of efficiency or the beneficial effects of improved stoichiometry. Hybrid stack configurations may also help to alleviate the higher pumping losses associated with ESFS stacks. Two examples of hybrid configurations are shown in Figures 10(a) and (b).

Conclusions

Optimizing any electrochemical system is necessary to obtain improved performance, durability, and cost-effectiveness. Various strategies have been explored experimentally and analytically in this work to optimize an EGSIS cell and stack. Employing a double-layer gas diffusion media with graded hydrophobicity facilitates water removal and reduces water accumulation inside the cathode catalyst layer. Similarly, using interdigitated and serpentine flow field channels on the cathode side improves transport of reactants and water management resulting in superior EGSIS performance compared to parallel channels. Operating conditions such as flow rate of the reactants and temperature should also be optimized. Furthermore, water management in EGSIS is important as both drying and flooding conditions can degrade performance. Two canonical configurations have been proposed for EGSIS stacks: ESFP and ESFS. Analysis reveals that the overall efficiency of the ESFP stack is higher than that of the ESFS stack. However, the ESFS stack may benefit from improved water management and performance enhancement due to higher stoichiometry. Hybrid designs that combine the features of ESFP and ESFS configurations may provide benefits in terms of higher efficiency, improved stoichiometry, or reduced pumping losses.

ACKNOWLEDGEMENTS

This work was supported by a grant from the Rapid Advancement in Process Intensification Deployment (RAPID) Manufacturing Institute. Portions of this manuscript were presented at the 2021 ASME International Mechanical Engineering Congress and Exposition[12].

REFERENCES

1. S. M. Summer, *Limiting Oxygen Concentration Required to Inert Jet Fuel Vapors Existing at Reduced Fuel Tank Pressures-final Phase*, (2004).

2. Federal Aviation Administraion, 76 (2008).

3. M. Burns and W. M. Cavage, *Inerting of a Vented Aircraft Fuelt Tank Test Article with Nitrogen-Enriched Air*, p. 29, Washington D.C., (2001).

4. C. A. Grande, *ISRN Chem. Eng.*, **2012**, 1–13 (2012).

5. W. F. Castle, *Int. J. Refrig.*, **25**, 158–172 (2002).

6. R. W. Baker, *Ind. Eng. Chem. Res.*, **41**, 1393–1411 (2002).

7. X. Feng, J. Ivory, and V. S. V. Rajan, *AIChE J.*, **45**, 2142–2152 (1999).

8. L. Reynolds, I. Eklund, and A. Haack, *Gas Sep. Technol.*, **2**, 9 (2001).

9. M. Wetterwald, C. P. Lawson, and J. K. W. Lam, *10th AIAA Aviat. Technol. Integr. Oper. Conf. 2010, ATIO 2010*, **2**, 1–11 (2010).

10. R. L. Johnson and J. B. Gillerman, *Aircraft fuel tank inerting system*, p. 259, Torrance, (1983).

11. U. R. Aryal, A. Chouhan, R. Darling, Z. Yang, M. L. Perry, and A. K. Prasad, *J. Power Sources*, **501**, 229959 (2021).

12. U. R. Aryal and A. K. Prasad, in *ASME International Mechanical Engineering Congress and Exposition, Proceedings (IMECE)*,, vol. 8A-2021, American Society of Mechanical Engineers Digital Collection (2022).

13. U. R. Aryal, M. Aziz, and A. K. Prasad, *J. Electrochem. Soc.* (2022).

14. R. M. Darling and M. L. Perry, (2017).

15. W. Schmittinger and A. Vahidi, *J. Power Sources*, **180**, 1–14 (2008).

16. A. Chouhan, B. Bahar, and A. K. Prasad, *Int. J. Hydrogen Energy*, **45**, 10991–10999 (2020).

17. B. H. Lim, E. H. Majlan, W. R. W. Daud, T. Husaini, and M. I. Rosli, *Ionics (Kiel).*, **22**, 301–316 (2016).

18. L. Berkeney, T. P. Fuller, J. Newman, and O. D. Co, *Water and Thermal Management in Solid-Polymer-Electrolyte Fuel Cells .... trn '1 0*, (1992).

19. M. Ji and Z. Wei, *Energies*, **2**, 1057–1106 (2009).

20. X. Li, I. Sabir, and J. Park, *J. Power Sources*, **163**, 933–942 (2007).

21. J. P. Feser, A. K. Prasad, and S. G. Advani, *J. Power Sources*, **161**, 404–412 (2006).

22. D. L. Wood, J. S. Yi, and T. V. Nguyen, *Electrochim. Acta*, **43**, 3795–3809 (1998).

23. Y. Wang, L. Wang, S. G. Advani, and A. K. Prasad, *J. Power Sources*, **292**, 39–48 (2015).

24. A. Z. Weber and R. M. Darling, *J. Power Sources*, **168**, 191–199 (2007).

25. X. Wang, X. Huang, L. J. Bonville, H. R. Kunz, M. L. Perry, and D. Condit, *J. Electrochem. Soc.*, **161** (2014).

26. Z. Wang, L. Qu, Y. Zeng, X. Guo, Z. Shao, and B. Yi, *RSC Adv.*, **8**, 1503–1510 (2018).

27. J. Larminie and A. Dicks, *Fuel Cell Systems Explained,* Second., p. 446, John Wiley & Sons Ltd, Chichester, West Sussex, (2003).

28. P. Majsztrik, A. Bocarsly, and J. Benziger, *J. Phys. Chem. B*, **112**, 16280–16289 (2008).

29. S. Motupally, A. J. Becker, and J. W. Weidner, *J. Electrochem. Soc.*, **147**, 3171 (2000).

30. T. E. Springer, T. A. Zawodzinski, and S. Gottesfeld, *J. Electrochem. Soc.*, **138**, 2334–2342 (1991).

31. P. W. Majsztrik, thesis, Princeton University (2008).

32. J. Lobato, P. Cañizares, M. A. Rodrigo, C. Ruiz-López, and J. J. Linares, *J. Appl. Electrochem.*, **38**, 793–802 (2008).

33. A. Jayakumar, S. P. Sethu, M. Ramos, J. Robertson, and A. Al-Jumaily, *Ionics (Kiel).*, **21**, 1–18 (2015).

34. D. P. Wilkinson, H. H. Voss, and K. Prater, *J. Power Sources*, **49**, 117–127 (1994).

35. P. Millet, R. Ngameni, S. A. Grigoriev, N. Mbemba, F. Brisset, A. Ranjbari, and C. Etiévant, *Int. J. Hydrogen Energy*, **35**, 5043–5052 (2010).

36. S. Siracusano, A. Di Blasi, V. Baglio, G. Brunaccini, N. Briguglio, A. Stassi, R. Ornelas, E. Trifoni, V. Antonucci, and A. S. Aric, *Int. J. Hydrogen Energy*, **36**, 3333–3339 (2011).

37. S. Siracusano, V. Baglio, N. Briguglio, G. Brunaccini, A. Di Blasi, A. Stassi, R. Ornelas, E. Trifoni, V. Antonucci, and A. S. Aricò, *Int. J. Hydrogen Energy*, **37**, 1939–1946 (2012).

38. Ö. F. Selamet, F. Becerikli, M. D. Mat, and Y. Kaplan, *Int. J. Hydrogen Energy*, **36**, 11480–11487 (2011).

39. K. Rashid, S. K. Dong, R. A. Khan, and S. H. Park, *J. Power Sources*, **327**, 638–652 (2016).

40. M. Riedel, M. P. Heddrich, and K. A. Friedrich, *Int. J. Hydrogen Energy*, **44**, 4570–4581 (2019).

41. A. Chouhan, U. R. Aryal, B. Bahar, and A. K. Prasad, *Int. J. Hydrogen Energy*, **45**, 31452–31465 (2020).

Accepted Manuscript
Version of record at: https://doi.org/10.1149/1945-7111/ac76e1

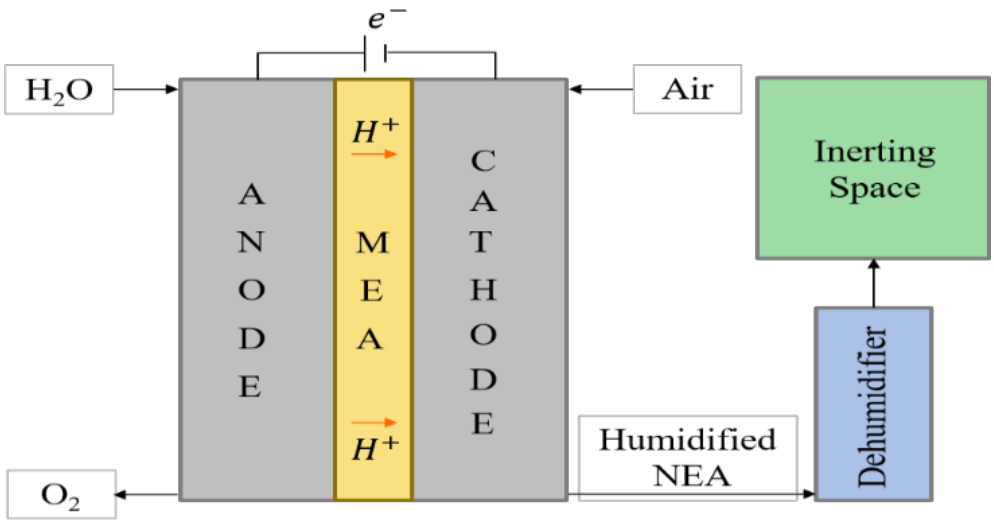

FIGURE 1. Schematic of an electrochemical gas separation and inerting system (EGSIS); adapted with permission from Aryal et al.[11].

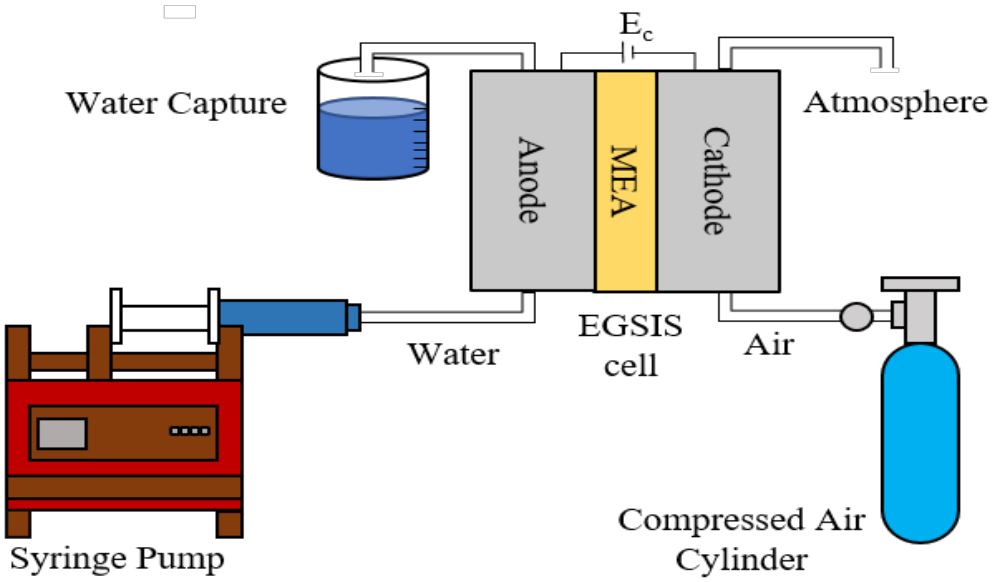

FIGURE 2. Schematic of experimental setup; adapted with permission from Aryal et al.[11].

Accepted Manuscript
Version of record at: https://doi.org/10.1149/1945-7111/ac76e1

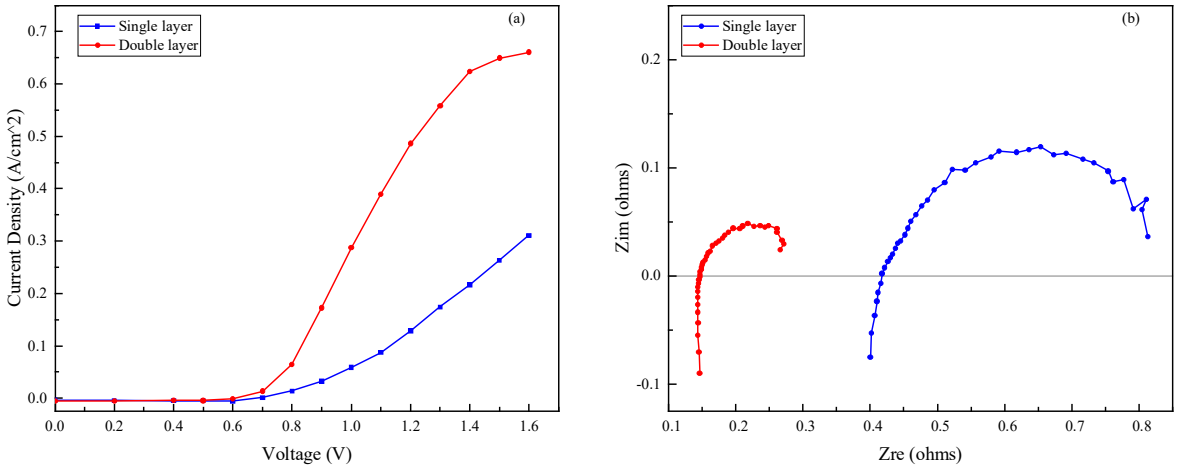

FIGURE 3. (a) Polarization curve, and (b) cell impedance measurement using EIS for single and double layer GDM

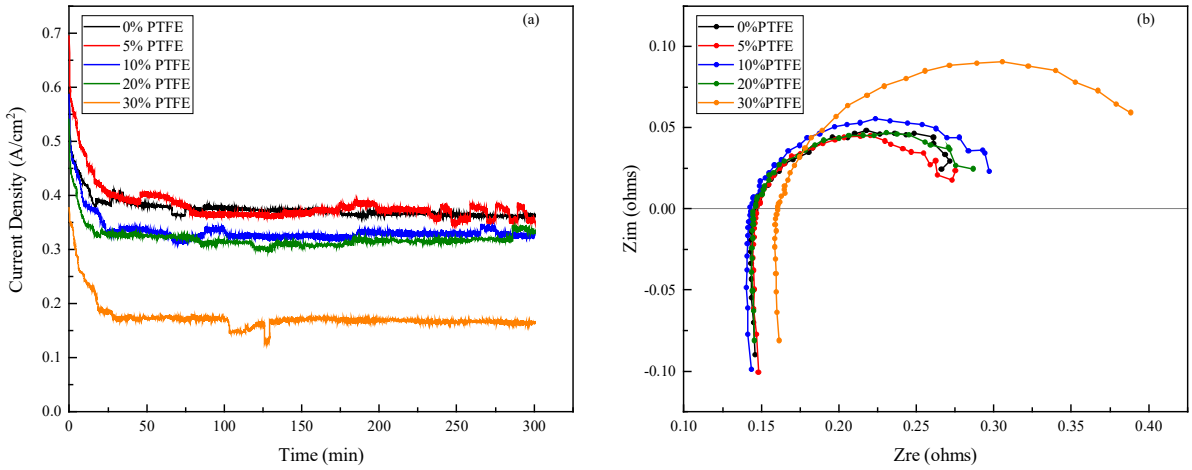

FIGURE 4. (a) Current density values at 1.5 V for double-layer cathode GDM at 60°C with 8 ml/hr of DI water supplied to the anode and 150 sccm of dry air to the cathode, and (b) cell impedance measurements using EIS for PTFE contents varying from 0 to 30% in the outer GDM layer.

Accepted Manuscript
Version of record at: https://doi.org/10.1149/1945-7111/ac76e1

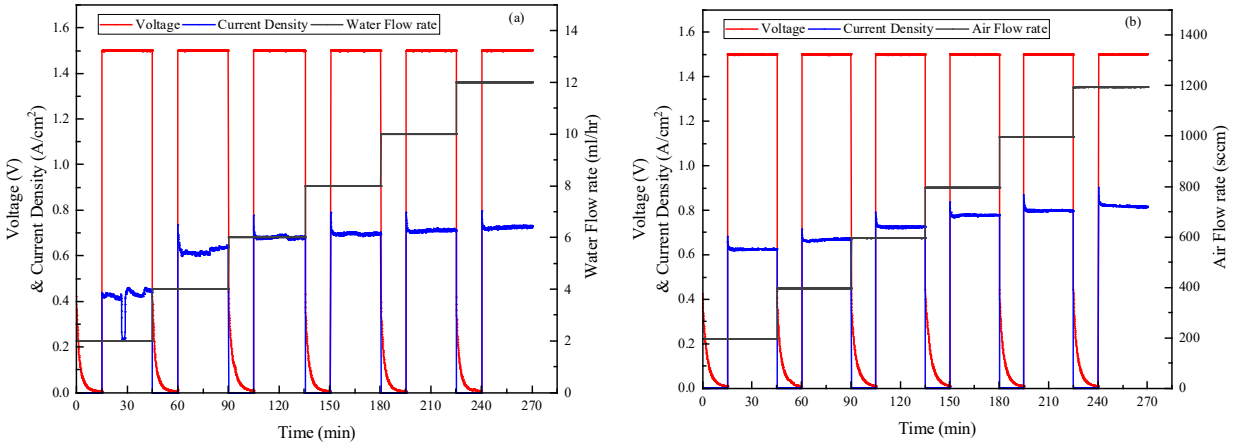

FIGURE 5. (a) Effect of anode water flowrate on current density at 80°C and 900 sccm cathode air flowrate, and (b) effect of cathode air flowrate on current density at 80°C for 8 ml/hr anode water flowrate

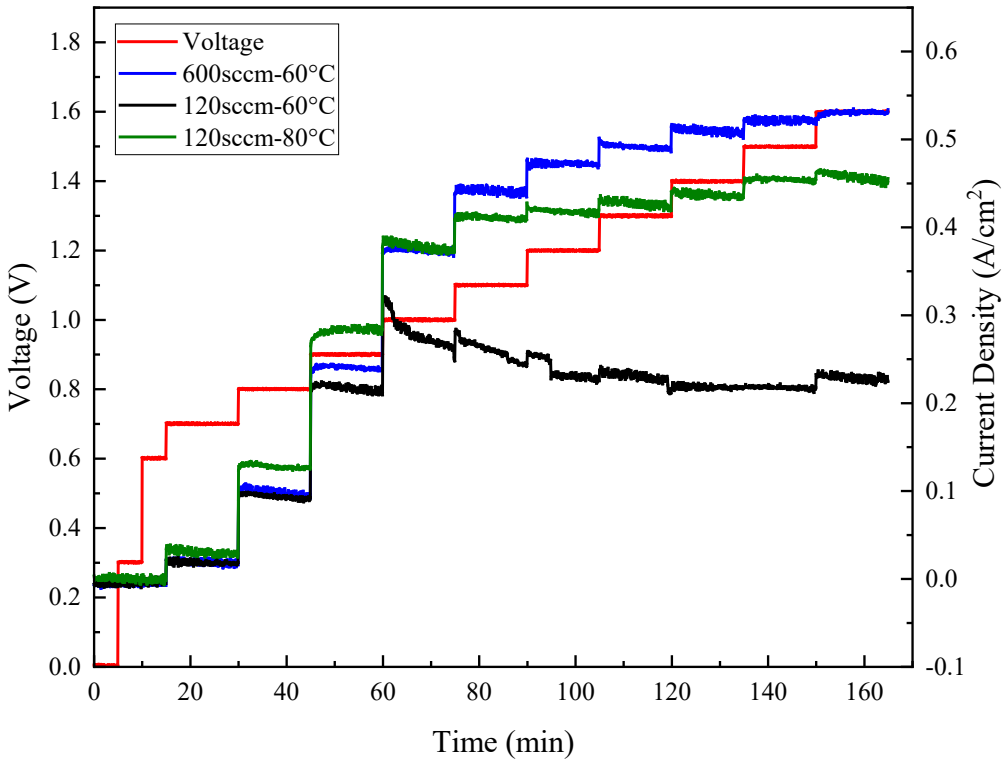

FIGURE 6. Comparison of current density values at two flow rates and temperatures

Accepted Manuscript
Version of record at: https://doi.org/10.1149/1945-7111/ac76e1

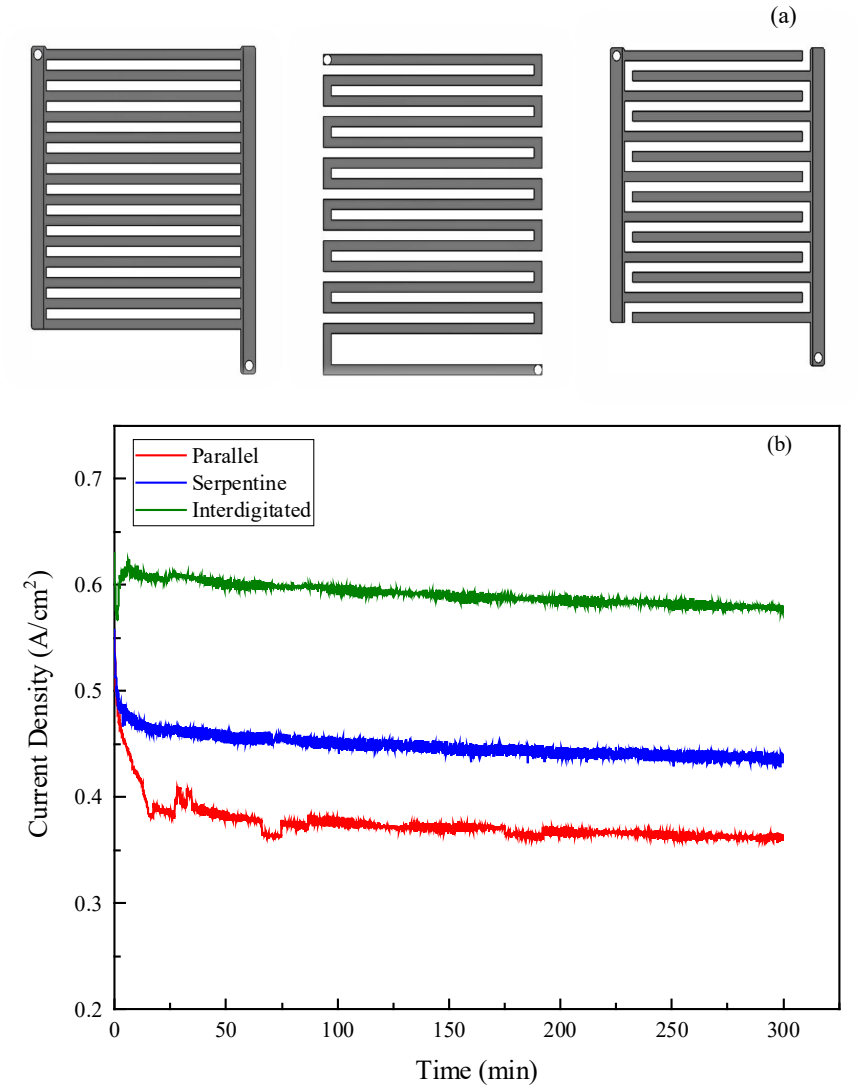

FIGURE 7. (a) Parallel, serpentine, and interdigitated (L to R) cathode flow field channels, and (b) current density for the three cathode flow field channels at 60°C for 8 ml/hr anode water flowrate and 150 sccm cathode air flowrate

Accepted Manuscript
Version of record at: https://doi.org/10.1149/1945-7111/ac76e1

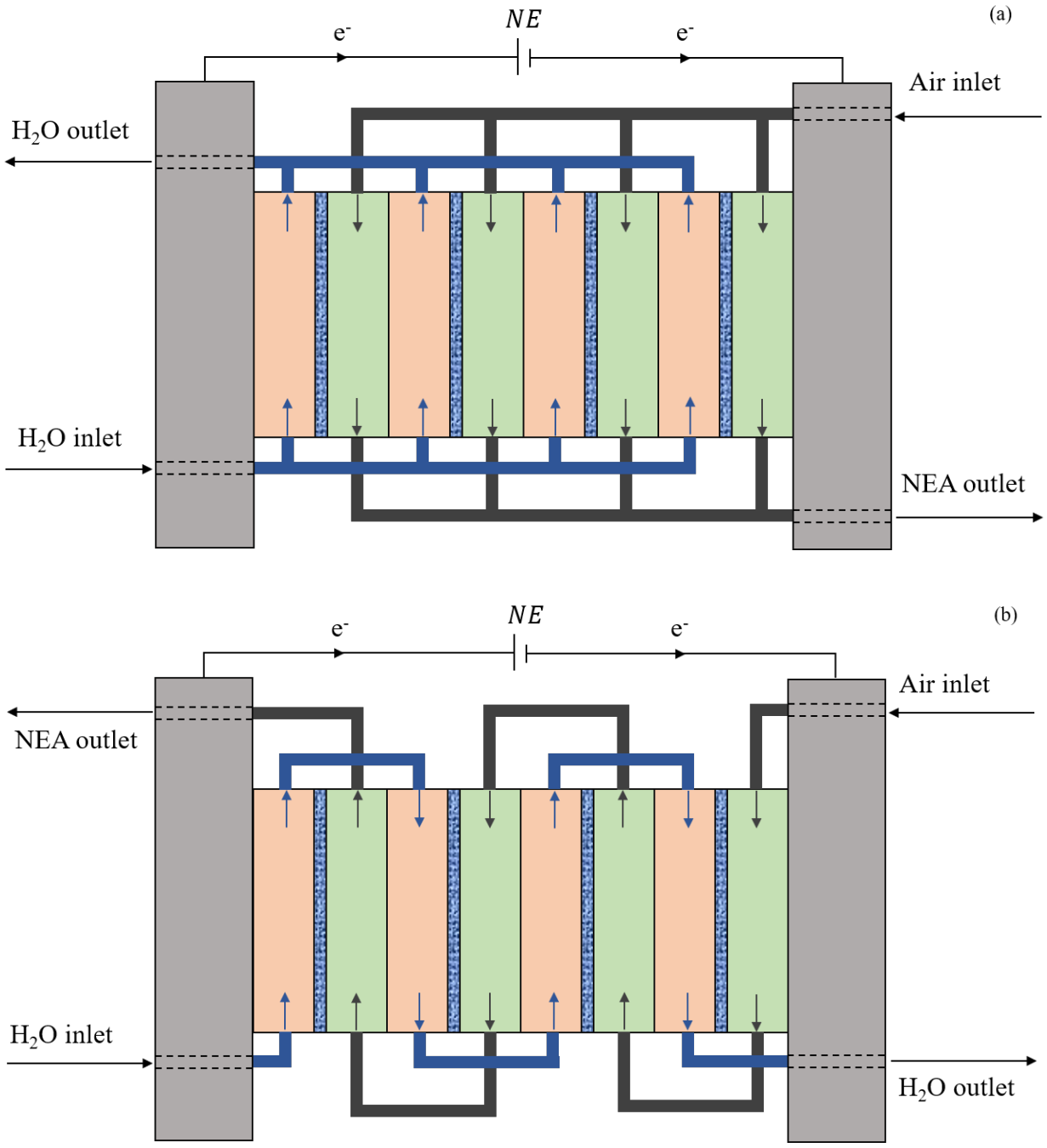

FIGURE 8. (a) Electrically in series/flow in parallel (ESFP), and (b) electrically in series/flow in series (ESFS) configurations

Accepted Manuscript
Version of record at: https://doi.org/10.1149/1945-7111/ac76e1

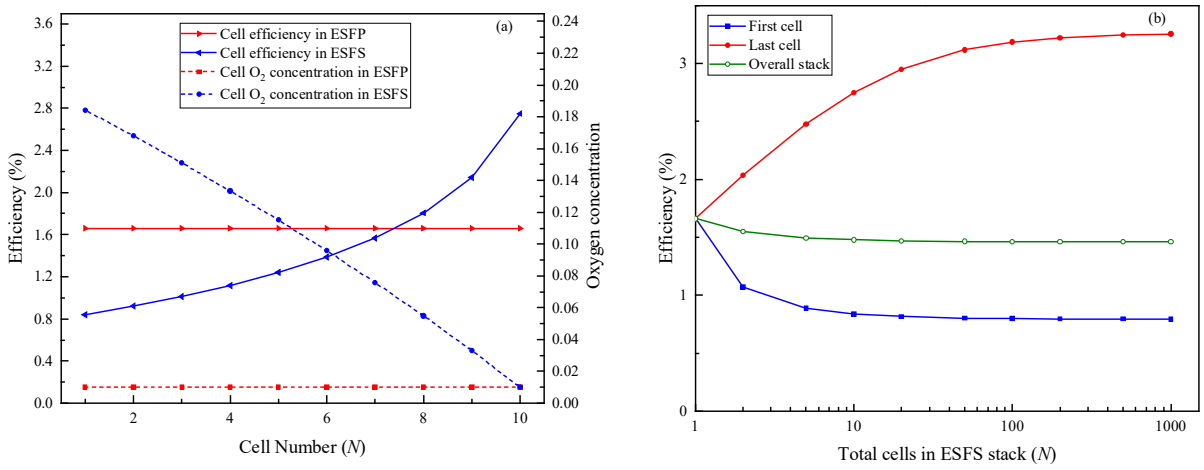

FIGURE 9. (a) Comparison of efficiency and NEA oxygen concentration for ESFP and ESFS stacks containing 10 cells, and (b) comparison of efficiency of the first cell, the last cell, and the overall stack with increasing number of cells for an ESFS stack

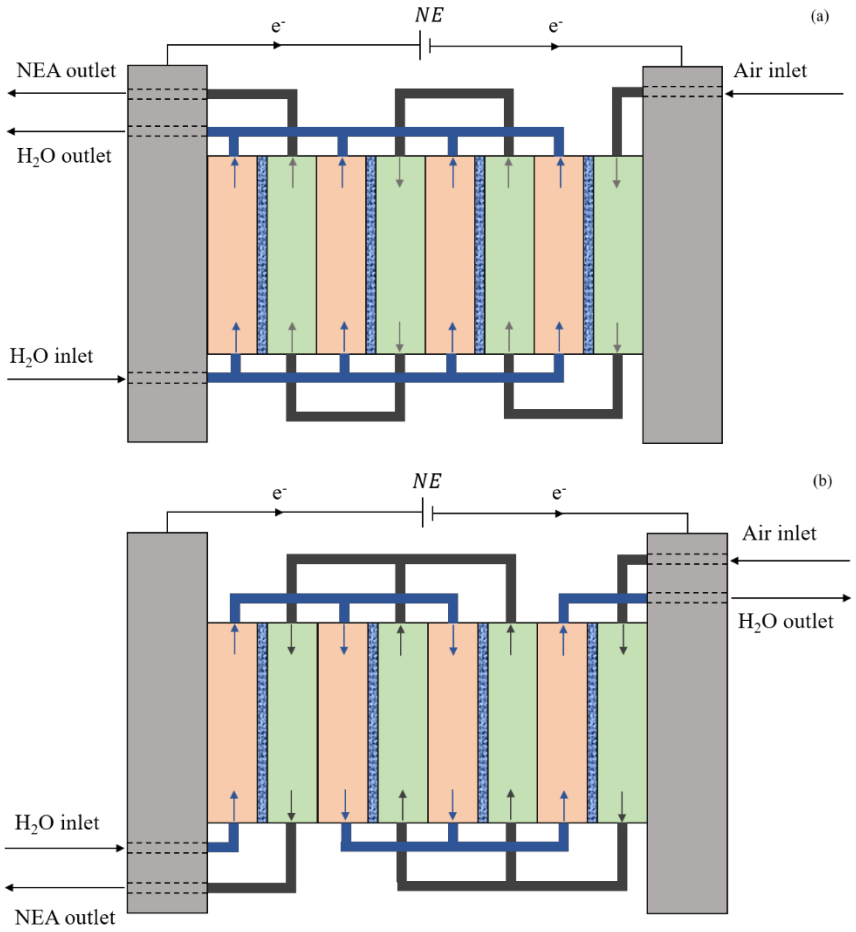

FIGURE 10. Examples of hybrid configurations